

# RA-NeRF: Robust Neural Radiance Field Reconstruction with Accurate Camera Pose Estimation under Complex Trajectories

Qingsong Yan<sup>1</sup>, Qiang Wang<sup>2,\*</sup>, Kaiyong Zhao<sup>3</sup>, Jie Chen<sup>4</sup>, Bo Li<sup>5</sup>, Xiaowen Chu<sup>6</sup> and Fei Deng<sup>1</sup>

**Abstract**—Neural Radiance Fields (NeRF) and 3D Gaussian Splatting (3DGS) have emerged as powerful tools for 3D reconstruction and SLAM tasks. However, their performance depends heavily on accurate camera pose priors. Existing approaches attempt to address this issue by introducing external constraints but fall short of achieving satisfactory accuracy, particularly when camera trajectories are complex. In this paper, we propose a novel method, RA-NeRF, capable of predicting highly accurate camera poses even with complex camera trajectories. Following the incremental pipeline, RA-NeRF reconstructs the scene using NeRF with photometric consistency and incorporates flow-driven pose regulation to enhance robustness during initialization and localization. Additionally, RA-NeRF employs an implicit pose filter to capture the camera movement pattern and eliminate the noise for pose estimation. To validate our method, we conduct extensive experiments on the Tanks&Temple dataset for standard evaluation, as well as the NeRFBuster dataset, which presents challenging camera pose trajectories. On both datasets, RA-NeRF achieves state-of-the-art results in both camera pose estimation and visual quality, demonstrating its effectiveness and robustness in scene reconstruction under complex pose trajectories.

## I. INTRODUCTION

Neural Radiance Fields (NeRF) [5] and 3D Gaussian Splatting (3DGS) [6] have shown remarkable performance in novel view synthesis, demonstrating great potential in dynamic scene representation [7], [8], surface reconstruction [9], [10], and large-scale reconstruction [11], [12], which are fundamental problems in robotics and autonomous driving. However, these methods rely heavily on accurate camera poses provided by traditional tools [13].

To address the above limitation, NeRFmm [14] and BARF [15] treat camera poses as learnable variables and unify camera pose estimation and scene reconstruction. To further improve reconstruction quality, SiRENmm [16] and GARF [17] replace the original ReLU activation function to preserve more information during the pose estimation. Additionally, L2G-NeRF [18] and LU-NeRF [19] adopt a local-to-global strategy for camera pose and scene reconstruction. Despite these improvements, these methods are primarily effective

<sup>1</sup>Qingsong Yan and Fei Deng are with School of Geodesy and Geomatics, Wuhan University, China [yanqs.whu@whu.edu.cn](mailto:yanqs.whu@whu.edu.cn), [fdeng@sgg.whu.edu.cn](mailto:fdeng@sgg.whu.edu.cn)

<sup>2</sup>Qiang Wang is with Department of Computer Science and Technology, HIT (Shenzhen), China [qiang.wang@hit.edu.cn](mailto:qiang.wang@hit.edu.cn)

<sup>3</sup>Kaiyong Zhao is with XGRIDS, China [kyzhao@xgrids.com](mailto:kyzhao@xgrids.com)

<sup>4</sup>Jie Chen is with Department of Computer Science, HKBU, China [chenjie@comp.hkbu.edu.cn](mailto:chenjie@comp.hkbu.edu.cn)

<sup>5</sup>Bo Li is with Department of Computer Science and Engineering, HKUST, China [bli@cse.ust.hk](mailto:bli@cse.ust.hk)

<sup>6</sup>Xiaowen Chu is with Data Science and Analytics Thrust, HKUST (Guangzhou), China [xwchu@ust.hk](mailto:xwchu@ust.hk)

\* indicates the corresponding author.

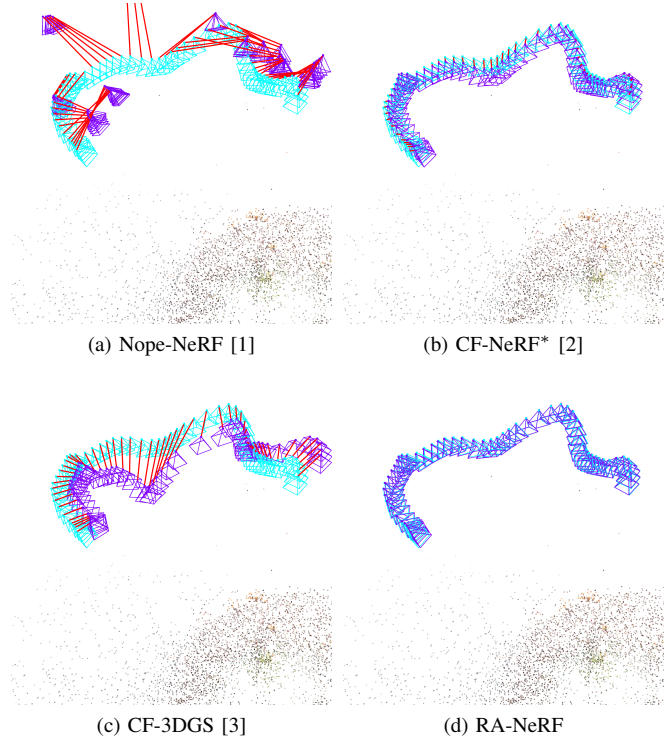


Fig. 1: Visualization of estimated camera poses for one scene from the NeRFBuster dataset [4]. The **ground truth** camera poses are obtained using COLMAP, while the **estimated results** are from Nope-NeRF [1], CF-NeRF [2], CF-3DGS [3], and our method RA-NeRF, where CF-NeRF\* means CF-NeRF does not estimate the focal length. The **line** indicates the error between the ground truth and the estimated poses.

for forward-looking scenes, such as scenes in the LLFF dataset [20], but struggle with scenes involving complex rotations when initial poses are unavailable.

A straightforward idea is to introduce external constraints to guide pose estimation. Nope-NeRF [1] and TD-NeRF [21] use depth [22] but need to deal with multi-view consistency. SC-NeRF [23], PoRF [24], and SPARF [25] utilize optical flow [26] or feature matching [27], but they require unreliable depth from NeRF to construct the loss. Alternatively, GNeRF [28] and IR-NeRF [29] assume known image distributions. DBARF [30] incorporates semantic information for pose estimation. However, these methods are prone to local minima, especially in scenes with significant rotations.

Inspired by incremental Structure-from-Motion (SfM) [13] and Simultaneous Localization and Mapping (SLAM) [31], LocalRF [32] and CF-NeRF [2] progressively reconstruct camera poses and 3D scenes from sequential images, lever-

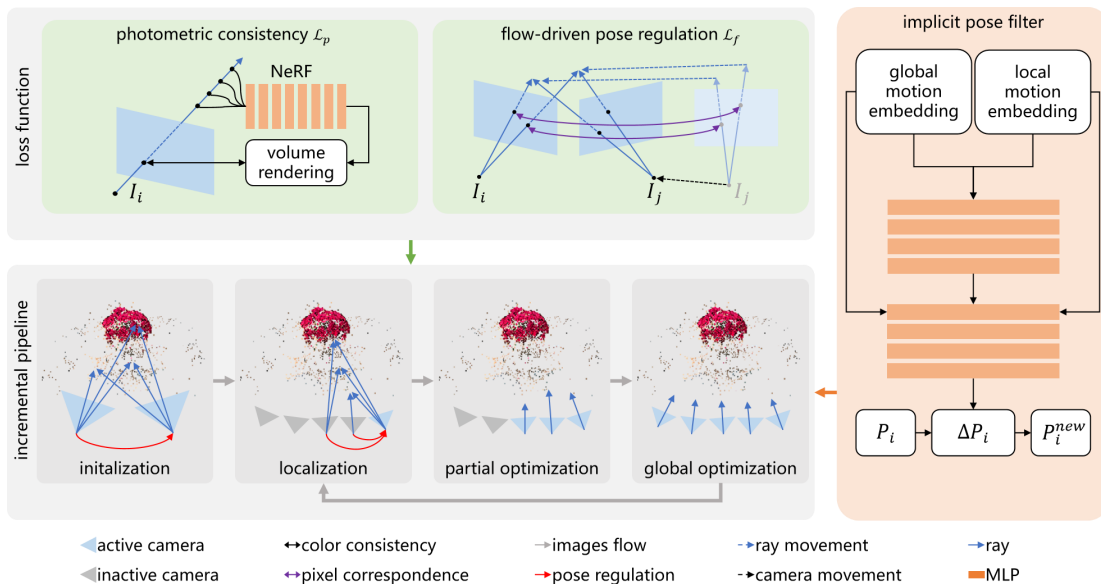


Fig. 2: The pipeline of the RA-NeRF, which uses photometric consistency to train the NeRF and camera poses, and improves reconstruction quality through flow-driven pose regulation and implicit pose filter.

aging initialization, localization, and optimization modules. In this process, initialization serves as the starting point, localization identifies the relative pose of newly added images, and optimization refines camera poses and the scene simultaneously. CT-NeRF [33] integrates optical flow [34] into the incremental pipeline, whereas CF-3DGS [3] uses depth priors [22]. Nonetheless, these methods still encounter challenges in achieving high-accuracy camera poses.

To address these issues, we propose a novel method, RA-NeRF, which accurately estimates camera poses from image sequences. RA-NeRF follows the incremental pipeline of CF-NeRF [2] and CF-3DGS [3]. Additionally, RA-NeRF employs flow-driven pose regulation to avoid convergence to local minima. Unlike existing methods that directly optimize camera poses, RA-NeRF leverages the implicit pose filter and updates camera poses in  $SE(3)$ . In Fig. 1, we compare the camera poses estimated by Nope-NeRF [1], CF-NeRF [2], CF-3DGS [3], and our method, RA-NeRF. The results demonstrate that the camera poses estimated by RA-NeRF are the closest to the ground truth generated by COLMAP [13]. Our contributions are as follows:

- 1) We propose a flow-driven pose regulation technique that significantly reduces the risk of converging to local minima during camera pose estimation.
- 2) We introduce an implicit pose filter capable of effectively modeling complex camera motions and mitigating noise from gradients, thereby enabling accurate pose estimation across diverse scenarios.
- 3) Experiments conducted on the NeRFBuster [4], [2] and Tanks&Temple [35], [1] datasets validate that RA-NeRF achieves state-of-the-art performance in terms of rendering quality and pose estimation on challenging trajectories with unknown camera poses.

## II. RELATED WORK

*a) NeRF and 3DGS:* NeRF [5] utilizes a multilayer perceptron (MLP) to implicitly reconstruct the 3D scene and

synthesize a high-quality novel view through volume rendering techniques. However, the efficiency of NeRF is limited by pixel-wise discrete sampling along each ray, motivating researchers to incorporate spatial priors for acceleration [36], [37]. Furthermore, NeRF struggles with unbounded scenes due to the sampling strategies [38]. In contrast, 3DGS [6] employs explicit 3D ellipsoids and uses rasterization for novel view synthesis. However, while 3DGS significantly improves reconstruction efficiency, it introduces the problem of over-reconstruction [39] and requires reducing model redundancy [40]. Meanwhile, MipNeRF [41] and Mip-Splatting [42] explore how to deal with artifacts caused by resolution changes. Moreover, [43], [44] attempt to maintain the reconstruction quality with sparse input images. On the other hand, [7], [8] try to reconstruct the dynamic scene by using time as a separate dimension, thus presenting richer information for users. Considering representing a large-scale 3D scene, [11], [12] split the whole scene into smaller pieces and merge them during visualization. Both NeRF and 3DGS have demonstrated impressive results in visual quality, and they also achieve significant results in surface reconstruction. [45], [46] reconstruct surface through modeling the relationship between transparency and the SDF, while [9] improve surface reconstruction efficiency based on Instant-NGP [37]. In addition to this, [47] conduct surface reconstruction based on 3DGS. To improve reconstruction quality, [48] explore how to reconstruct the surface under sparse views, and [10] introduces external constraints. Despite their successes, these methods depend heavily on accurate camera poses obtained from traditional methods [13], which splits the reconstruction pipeline into two distinct stages.

*b) Camera Pose Estimation:* Building on advancements in SfM [13] and SLAM [31], several works have attempted to estimate camera poses using NeRF and 3DGS. The simplest application of this idea is to determine the pose of a new image given a pre-trained NeRF [49]. Moreover, NeRFmm

[14] directly takes camera poses as learnable parameters, and is able to reconstruct both the scene and camera poses in forward-looking scenes. Based on this, SiRENmm [16] and GARF [17] replace ReLU in NeRF with functions such as sin or gaussian, to improve the quality of the pose estimation, while BARF [15] uses position embedding with the coarse-to-fine strategy. L2G-NeRF [18] and LU-NeRF [19] use the local-to-global strategy. However, the above methods only rely on the photometric consistency, and the pose quality is still not high. [50], [29] assume that the distribution of image poses is known, while [23], [1], [25] use the prior information such as the depth or optical flow. In recent years, LocalRF [32] and CF-NeRF [2] use incremental pipelines to reconstruct not only forward-looking but also rotating scenes. CT-NeRF [33] uses optical flow, and CF-3DGS [3] uses the depth as constraints during the incremental pipeline. In addition, [51] focus on generalization representation but do not focus on quality of camera poses. In conclusion, although the above methods achieve good results in reconstruction, they either only handle forward-looking scenes or require initial poses or prior information, and make it challenging to obtain high-quality camera poses in the case of complex motion trajectories. To address this problem, this paper proposes RA-NeRF, which can reconstruct high-accurate camera poses under the incremental pipeline using flow-driven pose regularization of camera poses and noise suppression by implicit pose filter.

### III. METHOD

In this section, we begin by introducing the fundamentals of photometric consistent. Next, we present the core techniques of RA-NeRF, flow-driven pose regulation and implicit pose filter, that enhance the accuracy of pose estimation. Finally, we describe the incremental learning pipeline of RA-NeRF, which integrates these components to simultaneously reconstruct neural implicit representations and poses from unposed images. The overall framework of RA-NeRF is illustrated in Fig. 2.

#### A. Photometric Consistency with NeRF

Given a collection of images  $\mathcal{I} = I_1, I_2, I_3, \dots, I_N$ , RA-NeRF needs to reconstruct the NeRF model  $\mathcal{F}$  and estimate camera poses  $\mathcal{P} = P_1, P_2, P_3, \dots, P_N$ , where  $P_i$  includes camera translation  $T_i$  and camera rotation  $R_i$  for the image  $I_i$ . Following BARF [15], CF-NeRF [2], and SPARF [25],  $\mathcal{F}$  does not use the positional encoding and the fine network with hierarchical volume sampling during the pose estimation.  $\mathcal{F}$  consists of 8 density MLP layers of width 256, using the ReLU activation function with inputs of 3D points and view directions. For a pixel  $p_i$  in  $I_i$  with the color  $c_{p_i}$ , the ray  $r_{p_i}$  can be obtained through  $p_i \sim K(R_i P + T_i)$ , according to the inverse process of projection.

To render the color  $\hat{c}_{p_i}$  of  $p_i$ ,  $\mathcal{F}$  first uniformly samples points along  $r_{p_i}$  with a given nearest depth  $d_{min}$  and farthest depth  $d_{max}$ , then predicts color  $c$  and density  $\sigma$  of these points, and finally generates  $\hat{c}_{p_i}$  through volume rendering. As the volume rendering is differentiable and treating  $\mathcal{F}$  and

$\mathcal{P}$  as learnable parameters, RA-NeRF can reconstruct  $\mathcal{F}$  and estimate  $\mathcal{P}$  simultaneously by minimizing the photometric inconsistency as Eq. 1 shows.

$$\mathcal{L}_p = \sum_{p \in \mathcal{I}} \|c_p - \hat{c}_p\| \quad (1)$$

#### B. Flow-driven Pose Regulation

However, the gradient of photometric consistency is not smooth, and can easily fall into local minima. Nope-NeRF [1] and CF-3DGS [3] use depth to offer geometric cues for pose estimation but are facing issues with multi-view scale inconsistency. Meanwhile, SC-NeRF [23], SPARF [25], PoRF [24], and CT-NeRF [33], on the other hand, use optical flow to constrain the direction of convergence of camera poses, but either require an initial pose to construct the epipolar loss or depth to construct the re-projection error, and also face the problem of ambiguity as pointed out by LU-NeRF [19]. To address these issues, RA-NeRF introduces a flow-driven pose regulation based on optical flow, which calculates relative camera poses from the optical flow of an image pair using multi-view geometry and directly regulates corresponding camera poses.

Specifically, given an image pair  $\langle I_i, I_j \rangle \in \mathcal{I}$ , RA-NeRF first computes the optical flow  $M_{ij} = \{m_i, m_j\}$  by PDC-Net [26], where  $p_i$  and  $p_j$  are pixels on  $I_i$  and  $I_j$ , respectively. Then, RA-NeRF calculates the fundamental matrix  $F_{ij}$  for  $\langle I_i, I_j \rangle$  using the eight-point method [52] and converts  $F_{ij}$  to the essential matrix  $E_{ij}$  via  $E_{ij} = K_j^{-1} F_{ij} K_i^{-1}$ . Finally, RA-NeRF obtains the relative camera pose  $\hat{R}_{ij}$  and  $\hat{T}_{ij}$  by decomposing  $E_{ij}$  using SVD, and selects the valid solution by ensuring that the triangulated depth of matched pixels is positive. Meanwhile, RA-NeRF calculates the relative camera pose  $R_{ij} = R_j R_i^T, T_{ij} = T_j - R_{ij} T_i$  between  $I_i$  and  $I_j$  from  $P_i$  and  $P_j$ .

It is important to note that  $E_{ij}$  can yield four potential relative camera poses, as shown in Fig. 3, where (a) and (d) are ambiguities pointed out by LU-NeRF [19]. Projected ray distance [23] and Sampson distance [53] cannot avoid this ambiguity and cannot calculate  $E_{ij}$  when  $P_i = P_j$  as  $T_{ij} = 0$ . However, directly calculating the relative camera pose does not suffer from these problems.

When the estimated camera poses  $\mathcal{P}$  are close to the ground truth, the differences between  $(R_{ij}, T_{ij})$  and  $(\hat{R}_{ij}, \hat{T}_{ij})$  should be minimal. However, as RA-NeRF estimates camera poses from scratch, the initial difference between  $(R_{ij}, T_{ij})$  and  $(\hat{R}_{ij}, \hat{T}_{ij})$  is substantial. To mitigate this, RA-NeRF regulates the estimated camera poses by directly minimizing the difference between these relative camera poses, as shown in Eq. 2. Notably, due to the absence of an absolute scale for the relative translation, RA-NeRF only regulates the direction of the translation vector.

$$\mathcal{L}_f = \left| \frac{T_{ij}}{\|T_{ij}\|} - \frac{\hat{T}_{ij}}{\|\hat{T}_{ij}\|} \right| + \lambda_r |R_{ij} - \hat{R}_{ij}| \quad (2)$$

Due to the large number of matching pixels between  $I_i$  and  $I_j$ , to reduce the computational complexity, RA-NeRF

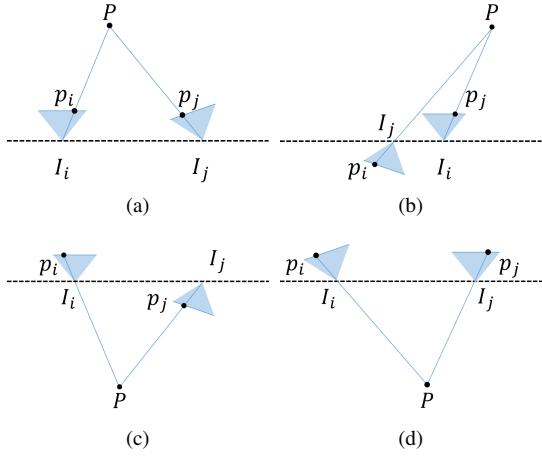


Fig. 3: Given the essential matrix  $E_{ij}$  of matched pixels  $p_i, p_j$ , we can decompose  $E_{ij}$  with four possible poses through multi-view geometry [54], which can mislead projected ray distance [23] and Sampson distance [53].

randomly selects a subset of the matching pixels in each iteration to compute the relative camera pose, using a strategy similar to RANSAC to improve efficiency and robustness.

### C. Implicit Pose Filter

Based on photometric consistency and flow-driven pose regulation, RA-NeRF can estimate camera poses from scratch. Similar to the importance of selecting a suitable way to estimate the rotation matrix during point cloud alignment [55], RA-NeRF updates camera poses in the Lie algebra  $\mathfrak{se}(3)$ , which represents the motion by a 6-dimensional vector [15], [18], and set it to learnable parameters. To estimate the camera pose of  $I_i \in \mathcal{I}$ , RA-NeRF starts from the initial pose  $P_i$  of  $I_i$ , and estimates the update values  $\Delta_i = (t_i, w_i)$ , which can be converted to  $\Delta P_i$  by Eq. 3, where  $e$  is the exponential map,  $w_i^{[\times]}$  is the skew symmetric matrix generated by  $w_i$ ,  $\theta_i = |w_i|$ , and  $V = I + w_i^{[\times]}(1 - \cos\theta_i)/\theta_i^2 + (w_i^{[\times]})^2(\theta_i - \sin\theta_i)/\theta_i^3$ . Finally, RA-NeRF obtains the new pose  $P_i^{new} = \Delta P_i \cdot P_i$ .

$$\Delta P_i = \begin{bmatrix} e^{w_i^{[\times]}} & V_i t_i \\ 0 & 1 \end{bmatrix} \quad (3)$$

If photometric consistency and flow-driven pose regulation were not affected by noise and provided consistently correct gradients for estimating  $\Delta_i$ , then  $P_i^{new}$  would be iteratively close to the ground truth pose. However, there are unreliaibilities in both the imaging process and the optical flow, and ignoring these noises will lead to inaccurate results.

To address this problem, RA-NeRF uses the implicit pose filter to deal with noise in gradients, which consists of an 8-layer MLP with a residual connection in the middle layer to enhance the learning capability, as Fig. 2 shows. The input of the implicit pose filter consists of a learnable global motion embedding of shape  $(1, 256)$ , and a learnable local motion embedding of shape  $(N, 256)$ , where  $N$  is the number of images. The output of the implicit pose filter is  $\Delta$  of shape  $(N, 6)$ . The global motion embedding represents the overall

motion pattern across all images, while the local motion embedding captures the unique motion state of each image.

### D. Incremental pipeline

RA-NeRF uses the incremental pipeline to avoid converging to local minima by estimating camera poses progressively, which contains initialization, localization, partial optimization, and global optimization, with enhancements from flow-driven pose regulation and implicit pose filter.

a) *Loss Function*: The loss function of RA-NeRF consists of two components, as shown in Eq. 4, where  $\mathcal{L}_p$  represents photometric consistency,  $\lambda_i$  and  $\lambda_f$  are weights for the flow-driven pose regulation.

$$\mathcal{L} = \mathcal{L}_p + \lambda_i \lambda_f \mathcal{L}_f \quad (4)$$

b) *Initialization*: Initialization is the first and most critical step in camera pose estimation, forming the foundation for subsequent processing. Instead of the complex strategies used in [19], [2], [33], RA-NeRF applies photometric consistency and flow-driven pose regulation during initialization. After setting all camera poses to the identity, RA-NeRF begins by randomly initializing the implicit pose filter and the NeRF model. Next, RA-NeRF selects the first  $N_{init} = 2$  images and estimates the camera pose using Eq. 4 with  $\xi_{iter}$  iterations, where  $\lambda_i = 1$ .

c) *Localization*: After initialization, RA-NeRF needs to determine the camera pose for a newly added image  $I_{new}$ . As NeRF performs poorly from viewpoints with no observations, RA-NeRF leverages both photometric consistency and flow-driven pose regulation for accurate localization. RA-NeRF first initializes the camera pose of  $I_{new}$  by previous image, then selects  $N_{loc}$  previous images  $\mathcal{I}_{loc}$ , reinitializes the implicit pose filter, reloads the NeRF model from the previous stage, computes the optical flow between  $I_{new}$  and  $\mathcal{I}_{loc}$ , fixes camera poses of  $\mathcal{I}_{loc}$ , and finally estimates the camera pose of  $I_{new}$  by Eq. 4 with  $\xi_{loc}$  iterations, where  $\lambda_i = 1$ . When  $N_{loc} \geq 2$ , the scale can be guaranteed to remain constant according to multi-view geometry [54].

d) *Optimization*: After localization, RA-NeRF performs partial optimization on  $I_{new}$  and previous  $N_{part}$  images with the NeRF model to minimize drift. When every  $N_{glob}$  new images are added, RA-NeRF performs global optimization on all images and the NeRF model. During optimization, RA-NeRF does not utilize the flow-driven pose regulation, as it is only effective for neighboring images and does not apply well to a larger set of images. Therefore, RA-NeRF uses Eq. 4 with  $\xi_{part}$  and  $\xi_{glob}$  iterations, where  $\lambda_i = 0$ . Besides, RA-NeRF reinitializes the implicit pose filter and reloads the NeRF model from the previous stage.

## IV. EXPERIMENTS

### A. Dataset

To thoroughly evaluate the performance of various pose estimation methods, we use two datasets: NeRFBuster [4], [2] and Tanks&Temple [35], [1]. The NeRFBuster dataset consists of 12 scenes, where most of scenes involve rotational

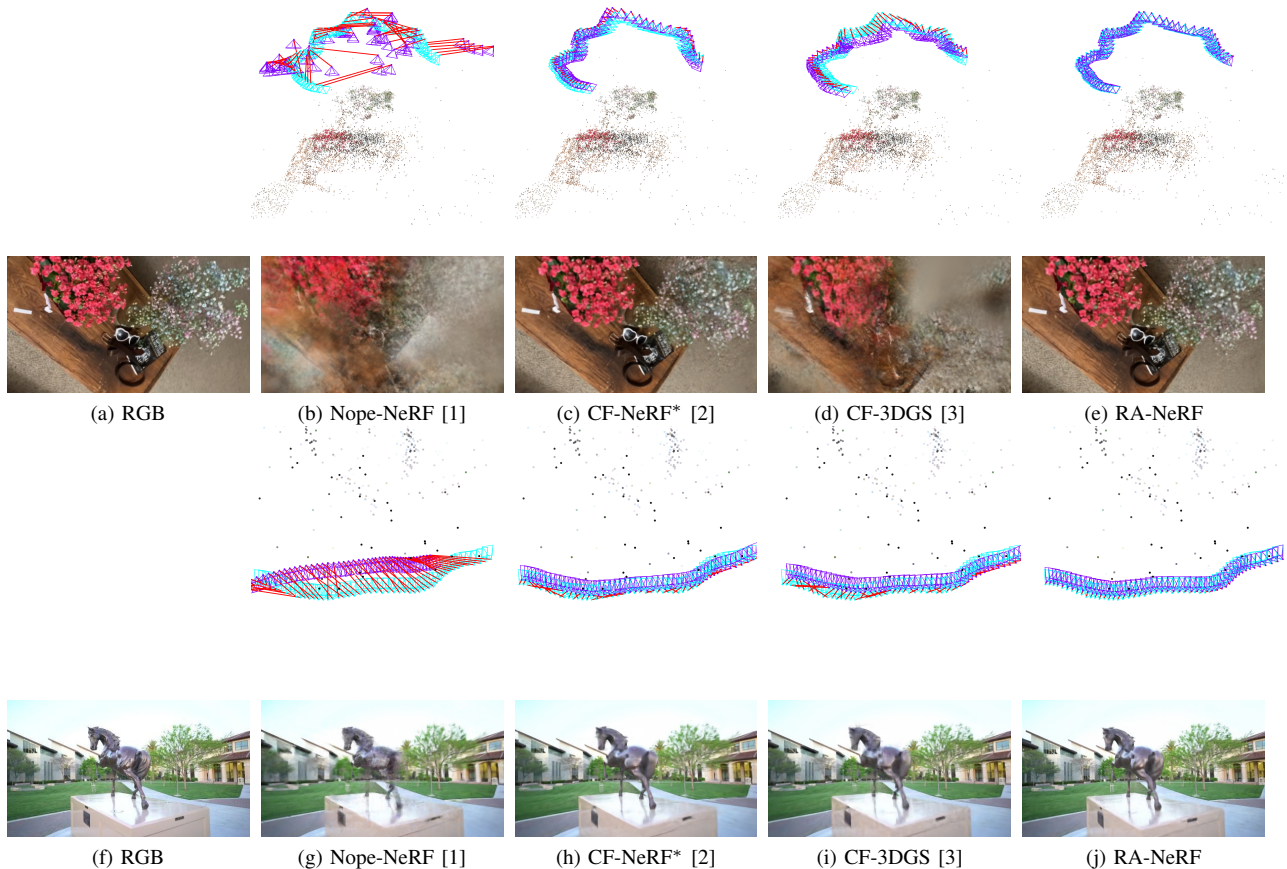


Fig. 4: Visualizations of estimated camera poses and rendering results. (a)-(e) are results from NeRFBuster [4] and (f)-(j) are results from Tanks&Temple [35].

motion around a central object and each scene includes approximately 50 images with a resolution of  $480 \times 270$ . The Tanks&Temple dataset comprises 8 real-world outdoor scenes, featuring a moving camera focused on a stationary object, where we uniformly sample around 50 images from each scene and resize them to a resolution of  $480 \times 270$ .

### B. Implementation

We implement RA-NeRF using Pytorch with the Adam [56]. On the NeRFBuster, we set the initial learning rate to  $5e^{-4}$  and set  $\lambda_f = 1e^{-1}$ . For the Tanks&Temple, we initialize the learning rate to  $5e^{-4}$ , and set  $\lambda_f = 1e^{-3}$ . Regarding other hyper-parameters, we set  $\xi_{loca} = 1100$ ,  $\xi_{init} = \xi_{part} = \xi_{glob} = 3100$ ,  $N_{init} = N_{loc} = 2$ ,  $N_{part} = N_{glob} = 5$ , and  $\lambda_r = 3$ . All experiments are conducted on an NVIDIA RTX 3090 GPU.

### C. Evaluation

We evaluate camera poses of different methods using rotation error  $\Delta R$  and translation error  $\Delta T$ . To calculate  $\Delta R$  and  $\Delta T$ , we first align estimated camera centers with ground truth camera centers via a similarity transformation. Then, we calculate the average Euler distance between translation vectors, and the average geodesic distance on the 3D manifold of rotation matrices. Note that as we try to estimate camera poses for all images from scratch, we calculate  $\Delta R$  and  $\Delta T$  for all images. To further compare the quality of

camera poses and avoid the influence of different network structures, we uniformly use the NeRFacc [57] to evaluate novel view synthesis, where PSNR and LPIPS are calculated, where we sample one image for testing every eight images and use the remaining images for training.

### D. Results

*a) NeRFBuster:* Tab. I presents the quantitative results on the NeRFBuster dataset. Our method, RA-NeRF, achieves state-of-the-art performance across all metrics. NeRFmm [14], SiRENmm [16], BARF [15], GARF [17], L2G-NeRF [18], and Nope-NeRF [1] produce incorrect camera poses, with  $\Delta R$  exceeding  $50^\circ$ . These methods estimate camera poses for all images at once, leading to convergence to local minima when large rotation exists. Although CF-NeRF [2] and CF-3DGS [3] use the incremental pipeline, they do not obtain high-quality camera poses. CF-NeRF solely relies on photometric consistency, facing drifts with more images, and CF-3DGS rapidly converges on representation, falling into local minima. Fig. 4 visualizes the results of different methods for better comparison.

*b) Tanks&Temple:* Tab. II presents the results on the Tanks&Temple dataset. Unlike the results on NeRFBuster, the differences between methods are smaller in this case, as this dataset primarily involves translations between images, instead of rotations, making it easier for methods to estimate camera poses. However, it is still notable that CF-NeRF [2]

TABLE I: Quantitative results on the NeRF Buster dataset, characterized by large rotational motions. RA-NeRF achieves state-of-the-art results, outperforming NeRFmm [14], SiRENmm [16], BARF [15], GARF [17], L2G-NeRF [18], CF-NeRF [2], Nope-NeRF [1], and CF-3DGS [3]. The **best** results and the **second best** results are highlighted.

		Mean	aloc	art	car	century	flowers	garbage	picnic	pikachu	pipe	plant	roses	table
$\Delta R \downarrow$	NeRFmm	79.1905	149.0038	13.7975	62.8193	86.2631	93.8266	88.8254	52.0380	87.3465	43.8570	27.7722	104.0850	104.6515
	SiRENmm	81.2834	135.3456	12.4257	87.8376	94.5317	92.2866	60.5024	45.0568	26.7353	46.8526	133.9530	139.5724	100.3015
	BARF	77.6321	154.1543	14.7550	81.3786	64.2474	74.8855	75.4210	61.1011	33.5440	47.4349	88.8684	125.3059	110.4894
	GARF	80.3641	118.9543	14.4842	56.7652	72.6237	97.8492	71.9970	49.3072	34.3633	106.4186	101.3184	116.4942	123.7941
	L2G-NeRF	66.0287	65.7245	13.3651	31.8843	83.9665	78.3117	86.0642	60.9882	97.6565	23.4746	37.6566	81.5597	131.6929
	Nope-NeRF	56.1676	48.7694	9.2974	68.3788	38.7692	57.5804	73.8243	43.3736	23.8043	29.1478	154.0849	57.3135	69.6677
	CF-NeRF	9.1090	<u>2.5324</u>	18.7037	17.7240	<u>6.1463</u>	6.3273	8.5708	10.8273	<u>10.4663</u>	16.7156	4.4945	2.7300	<u>4.0700</u>
	CF-NeRF*	<u>7.0779</u>	4.5319	4.7976	9.0527	11.9256	<u>4.0435</u>	<u>3.2722</u>	13.4793	15.7543	<u>7.6741</u>	<u>3.1088</u>	<u>1.6278</u>	5.6671
	CF-3DGS	11.2151	16.6094	<u>3.8206</u>	<u>4.5792</u>	25.6687	12.8236	5.6919	<u>3.1399</u>	16.1435	5.3298	8.6912	19.8901	12.2740
	RA-NeRF	<b>1.1449</b>	<b>0.3978</b>	<b>0.9128</b>	<b>1.1209</b>	<b>0.6981</b>	<b>0.9752</b>	<b>1.4214</b>	<b>1.1002</b>	<b>2.6337</b>	<b>1.3986</b>	<b>0.5753</b>	<b>1.6909</b>	
	$\Delta T \downarrow$	NeRFmm	25.2413	25.2792	22.1417	37.1552	35.4295	25.7556	21.0362	16.8080	40.5621	9.4368	19.9647	24.1385
SiRENmm		25.4806	27.7864	23.4831	42.9243	39.9758	26.8198	16.4988	12.2677	5.3457	10.6975	46.4030	28.2898	25.2755
BARF		22.9426	19.7298	20.6491	42.3339	26.3996	20.6169	19.7850	11.4757	21.6042	16.1818	35.0209	19.0742	22.4406
GARF		21.4076	20.8661	22.9420	29.1316	28.2595	21.8617	18.2010	14.4922	13.3614	17.4009	38.9866	10.7209	20.6676
L2G-NeRF		19.9316	24.1720	13.1701	19.8383	26.8447	13.2949	16.8679	13.9380	43.4267	13.6629	18.5277	19.0983	16.3371
Nope-NeRF		21.1305	26.8229	18.2390	38.4676	11.5269	19.0489	33.5241	10.3129	11.6039	13.8901	34.0780	20.3076	15.7444
CF-NeRF		2.6209	1.1089	8.5884	4.9247	<u>1.4121</u>	1.4058	3.4755	<u>0.7476</u>	<u>0.9453</u>	5.8665	1.1983	0.8495	<u>0.9280</u>
CF-NeRF*		<u>1.8853</u>	<u>0.7474</u>	3.4286	2.1918	<u>2.0726</u>	<u>0.7475</u>	<u>2.3736</u>	4.0586	1.7166	<u>2.6637</u>	<u>0.6550</u>	<u>0.2803</u>	1.6879
CF-3DGS		3.6402	3.7368	<u>2.7370</u>	<u>1.5525</u>	6.6890	5.1875	5.9701	1.3189	1.8616	3.1326	2.1379	6.0114	3.3472
RA-NeRF		<b>0.5388</b>	<b>0.5255</b>	<b>0.6629</b>	<b>0.3912</b>	<b>0.1876</b>	<b>0.4147</b>	<b>1.1159</b>	<b>0.4917</b>	<b>0.4424</b>	<b>0.9627</b>	<b>0.2715</b>	<b>0.1954</b>	<b>0.8046</b>
PSNR $\uparrow$		NeRFmm	16.2421	19.5471	15.3702	14.9577	13.9959	16.6522	14.5127	15.7169	20.5398	17.0115	18.0459	14.7628
	SiRENmm	19.9123	22.8658	18.3452	20.6571	17.3565	18.8590	17.6743	20.6531	25.3286	20.5824	24.2302	15.6283	16.7668
	BARF	18.6288	21.9318	20.2260	17.1700	15.2268	17.5742	16.6950	19.3063	22.3343	19.8260	26.1715	13.5690	13.5144
	GARF	18.4584	21.7836	19.9415	17.1403	15.6205	17.5725	17.0494	19.2293	22.2954	17.8705	25.5554	13.9215	13.5205
	L2G-NeRF	17.9168	20.6768	19.2531	17.7929	15.2495	18.1073	14.2474	17.6790	21.3126	19.0025	19.5653	16.7540	15.3606
	Nope-NeRF	18.6676	22.8376	19.6087	19.8081	16.2612	16.0533	15.5310	18.9618	26.6462	18.7508	19.9893	15.4433	14.1197
	CF-NeRF	24.4286	27.3675	<u>26.7849</u>	22.5143	21.4383	21.8342	<u>24.3138</u>	21.8609	<u>31.9826</u>	<u>22.0737</u>	25.6636	25.6908	21.6181
	CF-NeRF*	<u>25.3464</u>	<u>27.8416</u>	25.2270	<u>23.3041</u>	<u>22.7553</u>	<u>23.0537</u>	24.0998	<u>23.1762</u>	29.4807	21.9553	<u>27.7628</u>	<u>27.0469</u>	<u>28.4531</u>
	CF-3DGS	22.0264	24.7383	25.3289	20.0736	18.6802	17.4669	20.8899	22.6554	30.3376	20.4041	24.1208	17.7880	21.8329
	RA-NeRF	<b>27.2538</b>	<b>30.7039</b>	<b>27.3680</b>	<b>24.7297</b>	<b>23.9631</b>	<b>25.0211</b>	<b>24.9725</b>	<b>24.6056</b>	<b>35.5195</b>	<b>23.2117</b>	<b>30.2112</b>	<b>28.2220</b>	<b>28.5171</b>
	LPIPS $\downarrow$	NeRFmm	0.5719	0.5326	0.4828	0.6275	0.6166	0.5955	0.5938	0.6013	0.4500	0.5588	0.5676	0.5939
SiRENmm		0.4546	0.4124	0.3853	0.4445	0.4883	0.5000	0.5331	0.4962	0.3295	0.4872	0.3406	0.5416	0.4961
BARF		0.4834	0.3229	0.3451	0.5336	0.5723	0.5704	0.5349	0.5213	0.3642	0.5039	0.3099	0.6203	0.6023
GARF		0.4879	0.3255	0.3595	0.5278	0.5459	0.5705	0.5398	0.5269	0.3615	0.5608	0.3145	0.6231	0.5985
L2G-NeRF		0.4920	0.4593	0.4249	0.5349	0.5434	0.5467	0.5670	0.5556	0.4306	0.4538	0.3851	0.4859	0.5169
Nope-NeRF		0.4927	0.4325	0.3595	0.4957	0.5188	0.6165	0.5601	0.5245	0.3536	0.5475	0.4287	0.5337	0.5414
CF-NeRF		0.3233	0.1838	<u>0.2256</u>	0.4027	0.3608	0.3973	0.3774	<u>0.4750</u>	<u>0.1642</u>	0.4573	0.2607	0.2774	0.2976
CF-NeRF*		<u>0.3029</u>	<u>0.1705</u>	0.2614	<u>0.3788</u>	<u>0.3340</u>	<u>0.3424</u>	<u>0.3444</u>	0.4789	0.2142	<u>0.4456</u>	<u>0.1774</u>	<u>0.2305</u>	<u>0.2567</u>
CF-3DGS		0.4130	0.3161	0.2817	0.4634	0.4886	0.5651	0.4201	0.4691	0.2099	0.4913	0.3512	0.4996	0.3993
RA-NeRF		<b>0.2452</b>	<b>0.1067</b>	<b>0.2175</b>	<b>0.3261</b>	<b>0.2877</b>	<b>0.2668</b>	<b>0.2908</b>	<b>0.4131</b>	<b>0.0907</b>	<b>0.3911</b>	<b>0.1286</b>	<b>0.1994</b>	<b>0.2234</b>

TABLE II: Quantitative results on the Tanks&Temple dataset. Compared with Nope-NeRF [1], CF-NeRF [2], and CF-3DGS [3], RA-NeRF demonstrates competitive performance. The **best** results and the **second best** results are highlighted.

		Mean	Ballroom	Barn	Church	Family	Francis	Horse	Ignatius	Museum
$\Delta R \downarrow$	Nope-NeRF	58.4816	2.0547	86.9369	145.0743	36.5905	<b>1.0759</b>	163.9675	<b>0.5542</b>	31.5989
	CF-NeRF*	42.9849	<u>1.6731</u>	2.4796	<u>4.1735</u>	171.8357	149.7760	<u>8.1537</u>	4.3137	<u>1.4737</u>
	CF-3DGS	<u>7.3920</u>	5.8610	<b>1.2757</b>	16.4354	1.4195	2.8036	15.1154	9.4398	6.7858
	RA-NeRF	<b>1.9624</b>	<b>0.5715</b>	<u>3.2061</u>	<b>1.3643</b>	<b>0.8255</b>	<u>1.2063</u>	<b>4.9746</b>	<u>1.5659</u>	<u>1.9846</u>
$\Delta T \downarrow$	Nope-NeRF	5.3545	<u>0.3392</u>	5.0315	10.9355	5.6915	<u>0.4558</u>	1.1147	<u>1.0528</u>	18.2152
	CF-NeRF*	<u>1.3925</u>	0.3562	0.5176	<u>1.4012</u>	2.1876	3.5242	<u>0.5243</u>	2.3502	<b>0.2789</b>
	CF-3DGS	2.2121	3.4263	<b>0.3804</b>	5.0196	<u>0.5425</u>	0.9336	2.0865	2.7147	2.5930
	RA-NeRF	<b>0.3910</b>	<b>0.2089</b>	<u>0.4641</u>	<b>0.4469</b>	<b>0.1833</b>	<b>0.2768</b>	<b>0.1767</b>	<b>0.8300</b>	<u>0.5463</u>
PSNR $\uparrow$	Nope-NeRF	27.3324	<b>31.4314</b>	24.5962	23.6906	25.9189	31.1863	24.2281	<b>29.3578</b>	28.2500
	CF-NeRF*	26.5533	26.3096	<u>25.6028</u>	27.2631	24.8720	26.9767	26.3777	25.9892	<u>29.0353</u>
	CF-3DGS	<u>27.6146</u>	26.3057	23.8152	<u>27.5475</u>	30.4484	30.6915	<u>26.6287</u>	26.9313	28.5483
	RA-NeRF	<b>29.8012</b>	<u>30.2495</u>	<b>25.9803</b>	<b>32.0474</b>	<b>30.4555</b>	<b>32.0424</b>	<b>28.2649</b>	<u>27.7772</u>	<b>31.5923</b>
LPIPS $\downarrow$	Nope-NeRF	0.2528	<b>0.0892</b>	0.4402	0.2429	0.3085	<b>0.2303</b>	0.3084	<b>0.2083</b>	0.1943
	CF-NeRF*	0.2628	0.1900	<u>0.3849</u>	<u>0.1353</u>	0.3225	0.3851	<u>0.2452</u>	0.2978	<u>0.1415</u>
	CF-3DGS	<u>0.2340</u>	0.2109	0.4076	0.1620	<b>0.1407</b>	0.2674	0.2461	0.2592	0.1781
	RA-NeRF	<b>0.1844</b>	0.1077	<b>0.3792</b>	<b>0.0773</b>	<u>0.1459</u>	<u>0.2350</u>	<b>0.1822</b>	<u>0.2521</u>	<b>0.0958</b>

and Nope-NeRF [1] fail on some scenes, as they converge to incorrect solutions highlighted by LU-NeRF [19]. RA-NeRF achieves state-of-the-art on most metrics, while CF-3DGS [3] ranks second. Fig. 4 visualizes the results of different methods for better comparison.

### E. Ablation

To demonstrate the effectiveness of the proposed method, we conduct ablation experiments. For clarity, we only report the mean values of the  $\Delta R$  and  $\Delta T$ . Throughout ablation experiments, we utilize the NeRF Buster dataset.

a) *Flow-driven pose regulation*: In the absence of an initial pose, photometric consistency by itself does not provide accurate gradient information and often leads to convergence to a local minimum. However, with the flow-driven pose regulation, RA-NeRF can obtain better initial camera poses. Tab. III presents the influences of the flow-driven pose regulation. Without flow-driven pose regulation, RA-NeRF struggles to converge on several scenes, yielding camera poses with significant errors. However, by integrating flow-driven pose regulation during the initialization and localization, RA-NeRF significantly enhances the precision

TABLE III: Impact of flow-driven pose regulation.  $\checkmark$  and  $\times$  indicate the use and non-use of flow-driven pose regulation.

	Method	flow-driven pose regulation	Mean
$\Delta R \downarrow$	RA-NeRF	$\times$	78.0355
		$\checkmark$	<b>1.1449</b>
$\Delta T \downarrow$	RA-NeRF	$\times$	20.9749
		$\checkmark$	<b>0.5388</b>

TABLE IV: Impact of implicit pose filter.  $\checkmark$  and  $\times$  indicate the use and non-use of the corresponding module, where direct refers to directly calculating gradients on  $\mathfrak{se}(3)$  vector.

	Method	direct	implicit		Mean
			local	global	
$\Delta R \downarrow$	RA-NeRF	$\checkmark$	$\times$	$\times$	8.8946
		$\times$	$\checkmark$	$\times$	1.5056
		$\checkmark$	$\checkmark$	$\checkmark$	1.1889
		$\times$	$\checkmark$	$\checkmark$	<b>1.1449</b>
$\Delta T \downarrow$	RA-NeRF	$\checkmark$	$\times$	$\times$	2.3920
		$\times$	$\checkmark$	$\times$	0.6179
		$\checkmark$	$\checkmark$	$\checkmark$	0.5815
		$\times$	$\checkmark$	$\checkmark$	<b>0.5388</b>

and robustness of pose estimation.

*b) Implicit pose filter:* To deal with noise from photometric consistency and flow-driven pose regulation, IF-NeRF proposes the implicit pose filter with local motion embedding and global motion embedding to update camera poses. In contrast, the straightforward solution is directly setting a six-dimensional  $\mathfrak{se}(3)$  vector as learnable parameters to estimate the pose. Tab. IV compares the influences of different methods. RA-NeRF gives the worst results when the  $\mathfrak{se}(3)$  vector is used directly. Even when we combine the direct and implicit methods, the results of RA-NeRF are still worse than the implicit method. In addition, we note that without using global motion embedding, RA-NeRF is unable to model the motion of the whole scene and still degrades the accuracy.

Meanwhile, we also investigate different strategies to update camera poses. In addition to updating the camera pose in  $\text{SE}(3)$ , another approach is to convert  $P_{init}$  to  $\mathfrak{se}(3)$ , then update it by adding  $\Delta\mathfrak{se}3$ , and finally convert it back to  $\text{SE}(3)$ . Tab. V shows that updating in  $\mathfrak{se}(3)$  yields worse results. Although  $\text{SE}(3)$  and  $\Delta\mathfrak{se}3$  are equivalent, there are multiple data transformations in  $\Delta\mathfrak{se}3$ , raising the risk of numerical computational instability.

### F. Limitation

Although RA-NeRF achieves state-of-the-art results in pose estimation, there are several limitations. On the one hand, RA-NeRF requires overlapping images to build pixel correspondences. On the other hand, RA-NeRF is built upon NeRF with high computation complexity. However, these limitations can be overcome by a robust matching method, such as Dust3R [58], and an efficient backbone, such as Instant-NGP [37] or 3DGS [6].

## V. CONCLUSION

In this paper, we propose RA-NeRF, a novel approach to estimate high quality camera poses from complex trajectories. Following the incremental pipeline, RA-NeRF combines photometric consistency and flow-driven pose regulation to avoid converging to local minima, and leverages the implicit

TABLE V: Impact of pose updating strategies.

	Method	pose update domain	Mean
$\Delta R \downarrow$	RA-NeRF	$\mathfrak{se}(3)$	5.5228
		$\text{SE}(3)$	<b>1.1449</b>
$\Delta T \downarrow$	RA-NeRF	$\mathfrak{se}(3)$	3.2336
		$\text{SE}(3)$	<b>0.5388</b>

pose filter to deal with noise in gradients and complex motions. Experiments on the NeRFBuster and Tanks&Temple demonstrate that RA-NeRF outperforms existing methods and achieves state-of-the-art results. In summary, RA-NeRF demonstrates that it is possible to obtain high-quality camera poses and presents a promising end-to-end pipeline to reconstruct the 3D scene from unposed images.

## REFERENCES

- [1] W. Bian, Z. Wang, K. Li, J.-W. Bian, and V. A. Prisacariu, “Nope-nerf: Optimising neural radiance field with no pose prior,” in *Proceedings of the IEEE/CVF Conference on Computer Vision and Pattern Recognition*, 2023, pp. 4160–4169.
- [2] Q. Yan, Q. Wang, K. Zhao, J. Chen, B. Li, X. Chu, and F. Deng, “Cf-nerf: Camera parameter free neural radiance fields with incremental learning,” in *Proceedings of the AAAI Conference on Artificial Intelligence*, vol. 38, no. 6, 2024, pp. 6440–6448.
- [3] Y. Fu, S. Liu, A. Kulkarni, J. Kautz, A. A. Efros, and X. Wang, “Colmap-free 3d gaussian splatting,” in *Proceedings of the IEEE/CVF Conference on Computer Vision and Pattern Recognition (CVPR)*, June 2024, pp. 20 796–20 805.
- [4] F. Warburg, E. Weber, M. Tancik, A. Holynski, and A. Kanazawa, “Nerfbusters: Removing ghostly artifacts from casually captured nerfs,” *arXiv preprint arXiv:2304.10532*, 2023.
- [5] B. Mildenhall, P. P. Srinivasan, M. Tancik, J. T. Barron, R. Ramamoorthi, and R. Ng, “Nerf: Representing scenes as neural radiance fields for view synthesis,” in *Computer Vision—ECCV 2020: 16th European Conference, Glasgow, UK, August 23–28, 2020, Proceedings, Part I*, 2020, pp. 405–421.
- [6] B. Kerbl, G. Kopanas, T. Leimkühler, and G. Drettakis, “3d gaussian splatting for real-time radiance field rendering,” *ACM Transactions on Graphics*, vol. 42, no. 4, July 2023.
- [7] A. Pumarola, E. Corona, G. Pons-Moll, and F. Moreno-Noguer, “D-nerf: Neural radiance fields for dynamic scenes,” in *Proceedings of the IEEE/CVF Conference on Computer Vision and Pattern Recognition*, 2021, pp. 10 318–10 327.
- [8] Z. Li, Q. Wang, F. Cole, R. Tucker, and N. Snavely, “Dynibar: Neural dynamic image-based rendering,” in *Proceedings of the IEEE/CVF Conference on Computer Vision and Pattern Recognition*, 2023.
- [9] Z. Li, T. Müller, A. Evans, R. H. Taylor, M. Unberath, M.-Y. Liu, and C.-H. Lin, “Neuralangelo: High-fidelity neural surface reconstruction,” in *Proceedings of the IEEE/CVF Conference on Computer Vision and Pattern Recognition*, 2023, pp. 8456–8465.
- [10] D. Chen, H. Li, W. Ye, Y. Wang, W. Xie, S. Zhai, N. Wang, H. Liu, H. Bao, and G. Zhang, “Pgsr: Planar-based gaussian splatting for efficient and high-fidelity surface reconstruction,” *arXiv preprint arXiv:2406.06521*, 2024.
- [11] M. Zhenxing and D. Xu, “Switch-nerf: Learning scene decomposition with mixture of experts for large-scale neural radiance fields,” in *International Conference on Learning Representations*, 2023.
- [12] J. Lin, Z. Li, X. Tang, J. Liu, S. Liu, J. Liu, Y. Lu, X. Wu, S. Xu, Y. Yan, *et al.*, “Vastgaussian: Vast 3d gaussians for large scene reconstruction,” in *Proceedings of the IEEE/CVF Conference on Computer Vision and Pattern Recognition*, 2024, pp. 5166–5175.
- [13] J. L. Schonberger and J.-M. Frahm, “Structure-from-motion revisited,” in *Proceedings of the IEEE conference on computer vision and pattern recognition*, 2016, pp. 4104–4113.
- [14] Z. Wang, S. Wu, W. Xie, M. Chen, and V. A. Prisacariu, “Nerf-: Neural radiance fields without known camera parameters,” *arXiv preprint arXiv:2102.07064*, 2021.
- [15] C.-H. Lin, W.-C. Ma, A. Torralba, and S. Lucey, “Barf: Bundle-adjusting neural radiance fields,” in *Proceedings of the IEEE/CVF International Conference on Computer Vision*, 2021, pp. 5741–5751.
- [16] J. Guo and A. Sherwood, “improved-nerfmm,” <https://github.com/ventusff/improved-nerfmm>, 2021.

- [17] S.-F. Chng, S. Ramasinghe, J. Sherrah, and S. Lucey, "Gaussian activated neural radiance fields for high fidelity reconstruction and pose estimation," in *European Conference on Computer Vision*. Springer, 2022, pp. 264–280.
- [18] Y. Chen, X. Chen, X. Wang, Q. Zhang, Y. Guo, Y. Shan, and F. Wang, "Local-to-global registration for bundle-adjusting neural radiance fields," in *Proceedings of the IEEE/CVF Conference on Computer Vision and Pattern Recognition*, 2023, pp. 8264–8273.
- [19] Z. Cheng, C. Esteves, V. Jampani, A. Kar, S. Maji, and A. Makadia, "Lu-nerf: Scene and pose estimation by synchronizing local unposed nerfs," in *Proceedings of the IEEE/CVF International Conference on Computer Vision*, 2023, pp. 18312–18321.
- [20] B. Mildenhall, P. P. Srinivasan, R. Ortiz-Cayon, N. K. Kalantari, R. Ramamoorthi, R. Ng, and A. Kar, "Local light field fusion: Practical view synthesis with prescriptive sampling guidelines," *ACM Transactions on Graphics (TOG)*, 2019.
- [21] Z. Tan, Z. Zhou, Y. Ge, Z. Wang, X. Chen, and D. Hu, "Td-nerf: Novel truncated depth prior for joint camera pose and neural radiance field optimization," in *2024 IEEE/RSJ International Conference on Intelligent Robots and Systems (IROS)*. IEEE, 2024, pp. 372–379.
- [22] R. Ranftl, A. Bochkovskiy, and V. Koltun, "Vision transformers for dense prediction," in *Proceedings of the IEEE/CVF international conference on computer vision*, 2021, pp. 12 179–12 188.
- [23] Y. Jeong, S. Ahn, C. Choy, A. Anandkumar, M. Cho, and J. Park, "Self-calibrating neural radiance fields," in *Proceedings of the IEEE/CVF International Conference on Computer Vision*, 2021, pp. 5846–5854.
- [24] J.-W. Bian, W. Bian, V. A. Prisacariu, and P. Torr, "Porf: Pose residual field for accurate neural surface reconstruction," *arXiv preprint arXiv:2310.07449*, 2023.
- [25] P. Truong, M.-J. Rakotosaona, F. Manhardt, and F. Tombari, "Sparf: Neural radiance fields from sparse and noisy poses," in *Proceedings of the IEEE/CVF Conference on Computer Vision and Pattern Recognition*, 2023, pp. 4190–4200.
- [26] P. Truong, M. Danelljan, L. Van Gool, and R. Timofte, "Learning accurate dense correspondences and when to trust them," in *Proceedings of the IEEE/CVF conference on computer vision and pattern recognition*, 2021, pp. 5714–5724.
- [27] J. Sun, Z. Shen, Y. Wang, H. Bao, and X. Zhou, "Loftr: Detector-free local feature matching with transformers," in *Proceedings of the IEEE/CVF conference on computer vision and pattern recognition*, 2021, pp. 8922–8931.
- [28] Q. Meng, A. Chen, H. Luo, M. Wu, H. Su, L. Xu, X. He, and J. Yu, "Gnerf: Gan-based neural radiance field without posed camera," in *Proceedings of the IEEE/CVF International Conference on Computer Vision*, 2021, pp. 6351–6361.
- [29] J. Zhang, F. Zhan, Y. Yu, K. Liu, R. Wu, X. Zhang, L. Shao, and S. Lu, "Pose-free neural radiance fields via implicit pose regularization," in *Proceedings of the IEEE/CVF International Conference on Computer Vision*, 2023, pp. 3534–3543.
- [30] Y. Chen and G. H. Lee, "Dbarf: Deep bundle-adjusting generalizable neural radiance fields," in *Proceedings of the IEEE/CVF Conference on Computer Vision and Pattern Recognition*, 2023, pp. 24–34.
- [31] Z. Teed and J. Deng, "Droid-slam: Deep visual slam for monocular, stereo, and rgb-d cameras," *Advances in neural information processing systems*, vol. 34, pp. 16 558–16 569, 2021.
- [32] A. Meuleman, Y.-L. Liu, C. Gao, J.-B. Huang, C. Kim, M. H. Kim, and J. Kopf, "Progressively optimized local radiance fields for robust view synthesis," in *Proceedings of the IEEE/CVF Conference on Computer Vision and Pattern Recognition*, 2023, pp. 16 539–16 548.
- [33] Y. Ran, Y. Li, Q. Ye, Y. Huo, Z. Bai, J. Sun, and J. Chen, "Ct-nerf: Incremental optimizing neural radiance field and poses with complex trajectory," *arXiv preprint arXiv:2404.13896*, 2024.
- [34] J. Edstedt, I. Athanasiadis, M. Wadenbäck, and M. Felsberg, "Dkm: Dense kernelized feature matching for geometry estimation," in *Proceedings of the IEEE/CVF Conference on Computer Vision and Pattern Recognition*, 2023, pp. 17 765–17 775.
- [35] A. Knapitsch, J. Park, Q.-Y. Zhou, and V. Koltun, "Tanks and temples: Benchmarking large-scale scene reconstruction," *ACM Transactions on Graphics (ToG)*, vol. 36, no. 4, pp. 1–13, 2017.
- [36] A. Yu, R. Li, M. Tancik, H. Li, R. Ng, and A. Kanazawa, "Plenotrees for real-time rendering of neural radiance fields," in *Proceedings of the IEEE/CVF International Conference on Computer Vision*, 2021, pp. 5752–5761.
- [37] T. Müller, A. Evans, C. Schied, and A. Keller, "Instant neural graphics primitives with a multiresolution hash encoding," *ACM Transactions on Graphics (ToG)*, vol. 41, no. 4, pp. 1–15, 2022.
- [38] J. T. Barron, B. Mildenhall, D. Verbin, P. P. Srinivasan, and P. Hedman, "Mip-nerf 360: Unbounded anti-aliased neural radiance fields," in *Proceedings of the IEEE/CVF Conference on Computer Vision and Pattern Recognition*, 2022, pp. 5470–5479.
- [39] J. Zhang, F. Zhan, M. Xu, S. Lu, and E. Xing, "Fregs: 3d gaussian splatting with progressive frequency regularization," in *Proceedings of the IEEE/CVF Conference on Computer Vision and Pattern Recognition*, 2024, pp. 21 424–21 433.
- [40] Z. Fan, K. Wang, K. Wen, Z. Zhu, D. Xu, and Z. Wang, "Lightgaussian: Unbounded 3d gaussian compression with 15x reduction and 200+ fps," *arXiv preprint arXiv:2311.17245*, 2023.
- [41] J. T. Barron, B. Mildenhall, M. Tancik, P. Hedman, R. Martin-Brualla, and P. P. Srinivasan, "Mip-nerf: A multiscale representation for anti-aliasing neural radiance fields," in *Proceedings of the IEEE/CVF International Conference on Computer Vision*, 2021, pp. 5855–5864.
- [42] Z. Yu, A. Chen, B. Huang, T. Sattler, and A. Geiger, "Mip-splatting: Alias-free 3d gaussian splatting," in *Proceedings of the IEEE/CVF Conference on Computer Vision and Pattern Recognition*, 2024, pp. 19 447–19 456.
- [43] A. Jain, M. Tancik, and P. Abbeel, "Putting nerf on a diet: Semantically consistent few-shot view synthesis," in *Proceedings of the IEEE/CVF International Conference on Computer Vision*, 2021, pp. 5885–5894.
- [44] J. Yang, M. Pavone, and Y. Wang, "Freenerf: Improving few-shot neural rendering with free frequency regularization," in *Proceedings of the IEEE/CVF conference on computer vision and pattern recognition*, 2023, pp. 8254–8263.
- [45] L. Yariv, J. Gu, Y. Kasten, and Y. Lipman, "Volume rendering of neural implicit surfaces," *Advances in Neural Information Processing Systems*, vol. 34, pp. 4805–4815, 2021.
- [46] P. Wang, L. Liu, Y. Liu, C. Theobalt, T. Komura, and W. Wang, "Neus: Learning neural implicit surfaces by volume rendering for multi-view reconstruction," *arXiv preprint arXiv:2106.10689*, 2021.
- [47] A. Guédon and V. Lepetit, "Sugar: Surface-aligned gaussian splatting for efficient 3d mesh reconstruction and high-quality mesh rendering," in *Proceedings of the IEEE/CVF Conference on Computer Vision and Pattern Recognition*, 2024, pp. 5354–5363.
- [48] Q. Fu, Q. Xu, Y. S. Ong, and W. Tao, "Geo-neus: Geometry-consistent neural implicit surfaces learning for multi-view reconstruction," *Advances in Neural Information Processing Systems*, vol. 35, pp. 3403–3416, 2022.
- [49] L. Yen-Chen, P. Florence, J. T. Barron, A. Rodriguez, P. Isola, and T.-Y. Lin, "inert: Inverting neural radiance fields for pose estimation," in *2021 IEEE/RSJ International Conference on Intelligent Robots and Systems (IROS)*. IEEE, 2021, pp. 1323–1330.
- [50] M. Boss, A. Engelhardt, A. Kar, Y. Li, D. Sun, J. T. Barron, H. Lensch, and V. Jampani, "Samurai: Shape and material from unconstrained real-world arbitrary image collections," *arXiv preprint arXiv:2205.15768*, 2022.
- [51] F. Tian, S. Du, and Y. Duan, "Mononerf: Learning a generalizable dynamic radiance field from monocular videos," in *Proceedings of the IEEE/CVF International Conference on Computer Vision*, 2023, pp. 17 903–17 913.
- [52] R. I. Hartley, "In defense of the eight-point algorithm," *IEEE Transactions on pattern analysis and machine intelligence*, vol. 19, no. 6, pp. 580–593, 1997.
- [53] M. E. Fathy, A. S. Hussein, and M. F. Tolba, "Fundamental matrix estimation: A study of error criteria," *Pattern Recognition Letters*, vol. 32, no. 2, pp. 383–391, 2011.
- [54] R. Hartley and A. Zisserman, *Multiple view geometry in computer vision*. Cambridge university press, 2003.
- [55] J. Chen, Y. Yin, T. Birdal, B. Chen, L. J. Guibas, and H. Wang, "Projective manifold gradient layer for deep rotation regression," in *Proceedings of the IEEE/CVF Conference on Computer Vision and Pattern Recognition*, 2022, pp. 6646–6655.
- [56] D. P. Kingma and J. Ba, "Adam: A method for stochastic optimization," *arXiv preprint arXiv:1412.6980*, 2014.
- [57] R. Li, M. Tancik, and A. Kanazawa, "Nerfacc: A general nerf acceleration toolbox," *arXiv preprint arXiv:2210.04847*, 2022.
- [58] S. Wang, V. Leroy, Y. Cabon, B. Chidlovskii, and J. Revaud, "Dust3r: Geometric 3d vision made easy," in *Proceedings of the IEEE/CVF Conference on Computer Vision and Pattern Recognition*, 2024, pp. 20 697–20 709.